Nanoscale

Nanoscale–resolved elasticity: contact mechanics for quantitative contact resonance atomic force microscopy

SCHOLARONE™
Manuscripts

Nanoscale–resolved elasticity: contact mechanics for quantitative contact resonance atomic force microscopy

A. M. Jakob,[a] **J. Buchwald,**[a] **B. Rauschenbach,**[a] **and S. G. Mayr** [*a,b,c]

Contact resonance atomic force microscopy (CR-AFM) constitutes a powerful approach for nanometerresolved mechanical characterization of surfaces. Yet, absolute accuracy is frequently impaired by *ad hoc* assumptions on the dynamic AFM cantilever characteristics as well as contact model. Within the present study, we clarify the detailed interplay of stress fields and geometries for full quantitative understanding, employing combined experimentalnumerical studies for real AFM probes. Concerning contact description, a two-parameter ansatz is utilized that takes tip geometries and their corresponding indentation moduli into account. Parameter sets obtained upon experimental data fitting for different tip blunting states, are discussed in terms of model-specific artificiality versus real contact physics at the nanoscale. Unveiling the underlying physics in detail, these findings pave the way for accurate characterization of nanomechanical properties with highest resolution.

1 Introduction

Since its introduction in 1986[1], Atomic Force Microscopy (AFM) has been dramatically enhanced and features multi-property surface investigation tools nowadays, going well beyond the initial intention of simple nano-scale topography mapping (see e.g.[2–4]). One such sub-technique is Contact Resonance Atomic Force Microscopy (CR-AFM)[4,5]. Making use of the AFM-probe's modal response behavior once loaded onto a specimen surface, it permits accurate mechanical surface investigations in order to determine elastic properties like the indentation modulus or the loss modulus of viscoelastic media[6–9]. Similar to other dynamic AFM-based techniques, the shift of the contact resonance frequency is related to force gradients rather than absolute forces thereby yielding an improved sensitivity compared to static indentation experiments. Moreover, the opportunity to excite higher order eigenmodes, comes along with an effective probe stiffening and yields ideal mechanical sensitivity even for high contact stiffness. Hence - despite ongoing development of competing AFM-based techniques[10] - CR-AFM still remains unchallenged when focusing on the surface elastic properties of hard inorganic matter in the GPa regime. Various recent investigations concerning local mechanical characteristics of nanostructures[11–14], thin films[15,16] and functional materials[17] would not be possible otherwise. CR-AFM requires a rigid contact to be established

between the AFM tip and the specimen. Upon loading, a stress field extends into both bodies and makes an analysis of the mechanical response possible – but it turns out to be the Achilles heel as well. Indeed, artifacts originating from the tip shape, abrasion and roughness features influence cantilever dynamics and thus the mechanical information extracted from the probe's vibrational characteristics[18]. Therefore, CR-AFM, which principally belongs to the group of standardless measuring techniques, requires the use of properly chosen reference samples with known elastic properties in order to eliminate or determine unknown parameters for calculations. Fundamental work of former studies within this field enhanced the significance and accuracy of CR-AFM notably[19,20]. Among many innovations, single-reference based (SR) analysis - commonly performed in earlier work - are increasingly discarded in favor of two- or multi-reference sample analysis[17,20,21]. According to Stan and Price[20], systematic errors of SR-analysis can be avoided, but new resulting fitting parameters such as the tip indentation modulus M_{tip} (necessary to extract reliable information about the specimen's elastic properties) turned out to deviate dramatically from bulk values, intuitively expected for the tip material (here silicon). This finding might be partially ascribed to an intrinsic amorphous oxide layer as well as amorphization processes within silicon tips upon wear-off[20,21]. Passeri et al. furthermore investigated the tip calibration procedure itself and focused on simplified cantilever models as well as their impact on fitting parameters like M_{tip} related to the utilized contact model[21]. In conclusion, they found that negligence of lateral forces acting on the AFM tip contribute to an underestimation of M_{tip}. The present study addresses this question again and puts under scrutiny the shape

[a] *Leibniz Institut für Oberflächenmodifizierung (IOM), Permoserstr. 15, Leipzig, Germany. E-mail: Alexander.Jakob@iom-leipzig.DE, Stefan.Mayr@IOM-Leipzig.DE*

[b] *Faculty of Physics and Earth Sciences, University of Leipzig.*

[c] *Translational Center for Regenerative Medicine (TRM), University of Leipzig, Germany.*

of the tip as well as its apparent stiffness and their impact on the mechanical response of given reference samples. Therefore, a combined approach based on CR-AFM experiments and extensive individual finite element analysis (FEA) calculations of utilized cantilevers and tips is used. The experimental part consists of systematic CR-AFM measurements of the first two vertical contact resonances on four reference samples by means of different AFM probe types and various tip blunting states. Similar investigations with probes exhibiting a thin protective DLC coating are performed as well.

2 Experimental details

### 2.1 Probe reconstruction and FEA modeling

The analytical approach behind quantitative CR-AFM investigations can be subdivided into two major tasks. The first consists of modeling the AFM probes eigenfrequency behavior under properly chosen boundary conditions (BCs) (see Fig. 1 a)). Once the tip is loaded onto a specimen surface, the cantilever-surface system may be regarded as a beam, rigidly fixed at its base end ($x = 0$) and coupled to a spring k at its free tip end ($x = l$). The spring constant k (contact stiffness) describes the elastic interaction between the tip and the surface according to Hooke's law[22] and may be connected to the specimen indentation modulus M_s via an appropriate contact model. This constitutes the second major task of data analysis as will be explained in the next section. Referring back to the simplified cantilever-surface system, a beam bending partial differential equation (PDE) approach[23]

$$\rho\,\ddot{u}(x,t) + \frac{Y\,b^2}{12}\,u''''(x,t) = 0 \qquad (1)$$

$$\text{(i)} \quad u(x=0) = 0 \,, \; \text{(ii)} \; u'(x=0) = 0$$

$$\text{(iii)} \quad u''(x=l) = 0 \,, \; \text{(iv)} \; \frac{Y\,b^3\,w}{4}\,u'''(x=l) = k\,u(x)$$

is used for analytical modeling and commonly applied in the CR-AFM community. The PDE is of fourth order and corresponding BCs (i)-(iv) derive from the aforementioned system configuration, where Y denotes the Young's modulus of the cantilever material, ρ is the corresponding mass density and probe geometry is determined by length l, thickness b and width w. The basic idea is to gain a functional relationship between resonance frequency f_i of a vertical bending eigenmode $u_i(x,t_0)$ and the contact stiffness k (dispersion relation) in order to ascribe the experimentally accessible contact resonance f_i to an associated k-value. Equation 1 has been extensively studied in the past, and various additional influences like cantilever tilt angle α with respect to sample surface, lateral contact coupling k_{lat} as well as tip height and its position relative to the beam end have been considered and discussed (e.g.[24]). Although quite handy and more
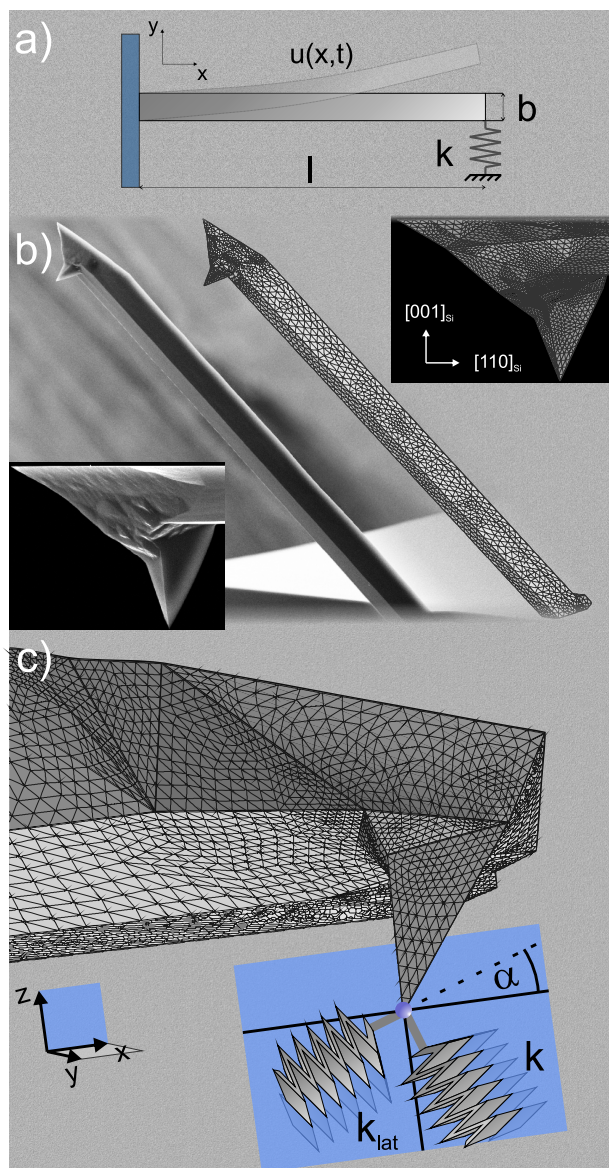
Fig. 1 Top: Simplest model describing a cantilever-surface interaction according to Eq. 1. Center: Exemplary SEM micrographs of a Tap190 cantilever and its reconstructed virtual counterpart. Bottom: Linear elastic probe-sample coupling is realized by contact stiffness k and an optional lateral shear component k_{lat}. A probe tilt angle $\alpha = 11°$ is considered as well. The illustrated probe resembles an NCLR cantilever type.

realistic than a harmonic-oscillator approximation, this two dimensional model yields some drawbacks arising from the simplified rectangular beam shape. This results in increasing discrepancies between predicted eigenmodes of higher orders and their counterparts of real complex-shaped cantilevers. The significance of calculated dispersion relations is in turn

Table 1 AFM probes used within the framework of this study. Associated free 1st and 2nd vertical eigenmodes are compared to predicted values based on numerical FEA computations. Individual effective cantilever stiffness k_c was extracted from stationary FEA calculations as well.

Probe	f_1/f_2 (Exp.) [kHz]	f_1/f_2 (FEA) [kHz]	k_c [N/m]	coating
NCLR-1	169.0 / 1036	169.0 / 1035.5	36.8	-
Tap190-1	165.4 / 1033	165.3 / 1032.0	42.7	-
Tap190-2	156.2 / 974	156.2 / 977.2	35.7	-
TapDLC-1	168.2 / 1044	168.2 / 1043.0	42.2	DLC
TapDLC-2	163.5 / 1019	163.5 / 1023.0	44.1	DLC

negatively affected. We therefore designed three-dimensional counterparts of utilized cantilever types and additionally optimized individual geometric features like the exact tip position as well as its shape. As exemplified in Fig. 1 b), images of AFM probes were first acquired from different perspectives (top, side) by means of scanning electron microscopy (SEM) and used for the digital reconstruction with computer assisted design software. Measurements are done with a Zeiss Ultra 55 field emission SEM ($U_{acc} = 15$ kV), where the integrated software measuring tool allowed accurate length determinations. We applied the COMSOL Multiphysics FEA software package to perform stationary and parametric eigenfrequency computations. Since FEA is a well elaborated tool applied in various fields of physics and engineering, an introduction into fundamentals of this computational technique is omitted at this point. The interested reader is referred to comprehensive textbook in this field[25]. The digital cantilever geometry was first splitted apart along its length axis and a symmetry condition was considered for the remaining cross sectional open surface. In fact, only one half of the probe was consequently modeled to obtain optimized effective mesh element densities. The meshing procedure involved 2 refinement steps in order to decrease local mesh size further at critical geometric features. The overall mesh element number typically amounts to about $70,000$ resulting in more than $200,000$ degrees of freedom and the elements are of Lagrange quadratic order. Anisotropic mechanical properties of the probe material are considered by an elasticity tensor ($C_{11} = 166$ GPa, $C_{12} = 64$ GPa, $C_{44} = 51$ GPa), which is furthermore properly rotated with respect to the global coordinate system and considers the growth orientation of single crystalline silicon AFM probe (see. Fig. 1 b))[26]. Fixation of the beam's base end was optimized to match that of real probes. As shown in Fig. 1 c) and explained for the analytical model, the probe-contact interaction occurs via contact stiffness k and an optional lateral spring k_{lat}, motivated by eventually occurring shear forces. Findings concerning the impact of the latter parameter are discussed later as well. Moreover, a cantilever tilt

angle $\alpha = 11°$ was used, accounting for the mounting of real probes in our AFM setup. Prior to computation of dispersion relations, the digital probe was slightly optimized in thickness to match both, the first and second free eigenmode of the real counterpart. A 30nm thick reflective Al coating - commonly attached to cantilever backsides - can be neglected for FEA simulations. Obtained discrepancies are listed in Table 1 and found below 0.4%. Dispersion relations of each probe are then acquired by parametrically solving the first two eigenfrequencies f_1 and f_2 for a discrete set of $k = 50...2000$ N/m. Data points are fitted by higher order polynomials to obtain corresponding $f_i(k)$ curves (see Fig.2). Stationary analysis revealed individual effective cantilever stiffness k_c. Therefore, a set of vertical constant forces in the range of $100 - 1000$ nN was applied to the tip, resulting in increasing deflections u_z along z-direction. The beam stiffness k_c finally results as the slope of $F(u_z)$. In this work, we focus on 5 probes listed in Table 1. One cantilever is a former version of the Nanosensors NCLR type, whereas the other four tips are all Budget Sensors Tap190Al and two being additionally equipped with a DLC coating of about 15 nm thickness - according to manufacturer specifications. Both AFM probe types are characterized by nominally similar stiffnesses (48 N/m) and first resonance frequencies (190 kHz), whereas both geometries nevertheless differ notably. The first mentioned especially features its tip to be much closer at the free end.
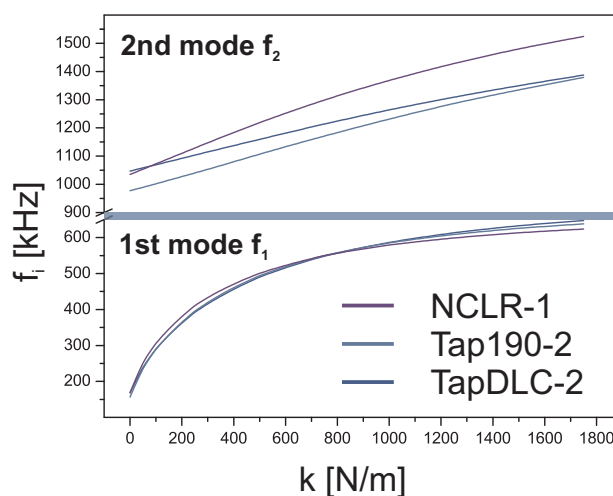
Fig. 2 Exemplary dispersion relations of the first two eigenmodes obtained for NCLR-1, Tap190-1 and TapDLC-2 using FEA and assuming $k_{lat} = 0$ N/m.

2.2 Contact model

As stated before, the contact model spans the bridge between contact stiffness k and the desired sample indentation modulus M_s. According to[19], we assumed a radially symmetric tip

profile of n-th polynomial order

$$z(r) = c\,r^n \tag{2}$$

From Hooke's law of linear elasticity, the indentation modulus M is generally defined as[27]

$$\frac{\partial F}{\partial u} = k := \frac{2}{\sqrt{\pi}} M \sqrt{A_c} \tag{3}$$

where A_c is the contact area of a loaded body and the prefactor corrects the more specified definition $k := 2 M a_c$ for a circular contact of radius a_c. Since the AFM tip material usually exhibits no superior rigidity compared to investigated samples, the contact stiffness k must be considered as superposition of two sub-springs k_{tip} and k_s in series. Accordingly, the tip-sample system indentation modulus M subdivides similarly

$$\frac{1}{M} = \frac{1}{M_{tip}} + \frac{1}{M_s} \tag{4}$$

Except for the special case of a flat punch tip, the contact area A_c depends in a non-trivial way on parameters like the tip shape profile and the loading force F_l applied to the indenter. A detailed calculation shall be omitted at this point, but following analytical procedure of Vlassak et al. for determination of a load functional $F_l(A_c)$[27] and assuming a tip profile given by Eq. 2, one ends up with

$$k = 2 M^{\frac{n}{n+1}} \left(\frac{(n+1)\,(1-\varepsilon^2)^{\frac{n}{4}}\,F_l}{c\,n\,(1+(-1)^n)\,(1+(1-\varepsilon^2)^{\frac{n}{2}})} \right)^{\frac{1}{n+1}} \tag{5}$$

where ε is the eccentricity of an elliptically shaped contact. Finally, the ratio k_x/k_y for two different tip-sample systems x and y amounts to

$$\frac{k_x}{k_y} = \left(\frac{M_x}{M_y} \right)^{\frac{n}{n+1}} \tag{6}$$

where the assumption $\varepsilon_x \approx \varepsilon_y$ is usually well fulfilled as long as mechanical anisotropies of both specimens x and y do no differ more than a few percent (which is the case for specimens used herein). Once a set $\{k_x;\ 1 < x \le N\}$ of N reference samples with given $M_{s,x}$ is known, Eq. 6 can be used to fit the data by adjusting the free parameters n and M_{tip}. The desired sample indentation modulus M_s of an unknown specimen is then finally accessible once corresponding k is determined from the measured f_i value and simulated dispersion relation. Note that for a parabolic tip ($n = 2$), the exponent in Eq. 6 equals $2/3$ - as in the case of a spherical Hertzian indenter[*]. The special case of a flat punch, where the contact area A_c remains always constant, can be achieved by $n \to \infty$.

---

[*] This is due to the fact, that literature approximates the Hertzian sphere with a second order polynom.

2.3 CR-AFM: Experimental details and specimens

Measurements were realized using a fully programmable Asylum Research MFP-3D AFM. All CR-AFM routines - allowing point-map data acquisition as well as continuous mechanical surface imaging - are self-designed utilizing the integrated Igor Pro programming language. For the quantitative study
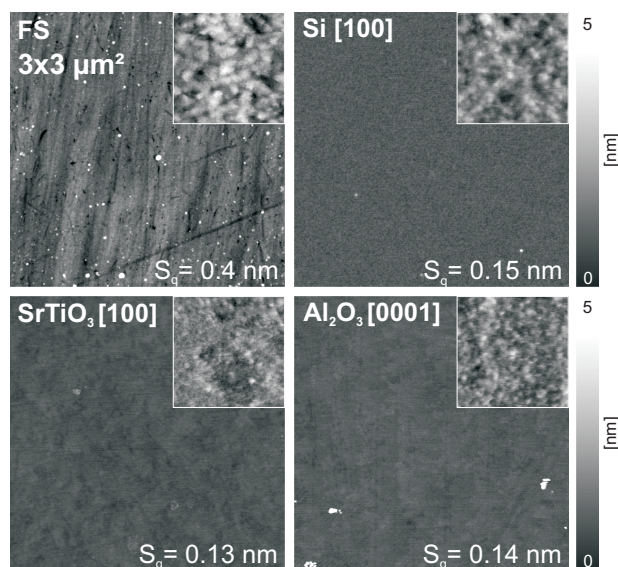
Fig. 3 Exemplary AFM micrographs on all four reference samples with a nominal resolution of 512×512 Pixel (about $6 - 7$ nm, depending on tip quality). Image processing (plane fit first order) and roughness calculations are done with the SPIP software[28], whereas small spike-like residuals were excluded for analysis. Insets show AFM scans of 100 nm lateral size using high resolution probes. Color coded height range amounts to 3 nm.

presented here, we measured contact resonance frequencies on four reference samples (FS - fused silica, Si - silicon, STO - SrTiO₃ and Sa - sapphire) listed in Table 2. The measuring procedure involved a cantilever excitation by means of a commercial AFM sample transducer attached below the specimens. Contact resonances f_i are identified via frequency sweeping and an integrated digital Lock-In amplifier - providing the excitation response spectrum of the cantilever-sample system. A standard Lorentz fit procedure finally yields the desired peak characteristics of f_i. For each specimen, a point map array of 5×4 measuring spots was chosen, whereas the contact resonance at each spot is a median of 7 sweeps and a specimen's representative value is the average of the whole point-map array. First and second contact resonances were successively measured. One cycle consists of a measuring series on all four reference samples, where the specimen measuring order of two subsequent cycles was inverted. Systematic errors between first- and second contact resonance acquisitions as well as artifacts due to abrasion can thus be

Table 2 Reference samples of interest and corresponding properties. Elastic constants are taken from literature and generally accepted values. The indentation modulus M_s refers to loading direction along crystal growth orientation (normal to surface plane). The quartz specimen is used for comparison of results obtained with DLC-coated tips.

Specimen	Orientation	Elastic constants [GPa]	M_s [GPa]
Fused silica (FS)	amorphous	-	75^{29}
Silicon (Si)	[100]	$C_{11} = 166, C_{12} = 64, C_{44} = 51\,^{30}$	165
SrTiO$_3$ (STO)	[100]	$C_{11} = 317.5, C_{12} = 102.5, C_{44} = 123.5\,^{31}$	298
Al$_2$O$_3$ (Sa)	[0001]	$C_{11} = 496, C_{12} = 164, C_{13} = 115, C_{33} = 498, C_{44} = 148\,^{32}$	433
Quartz (Qu)	[001]	-	125^{33}

avoided. Only if at least two consecutive cycles agreed within the experimental error of average point-map values (given by the standard deviation), gathered contact resonances were accepted as true representatives of each reference sample and used for further analysis. The macroscopic measuring position of each point-array cycle was randomly chosen and the array size amounts to 1×1 μm^2. Applied tip loads F_l onto specimen surfaces varied around $400 - 600$ nN in this study, depending on individual probe stiffness given in Table 1. Specific tip blunting, in order to investigate the influence of tip wear-off state on subsequent analysis, was carefully done by scanning small areas (300×300 nm^2) on a sapphire surface in contact mode. Two tip blunting states are distinguished for each probe herein. The initial one - yielding less wear-off - shall be denoted as "sharp" and the latter is called "blunted". All specimens are high quality single crystals (except amorphous fused silica) and grown/polished by CrysTec Kristalltechnologie GmbH. More details concerning mechanical and crystallographic properties can be taken from Table 2, where indentation moduli are computed from elastic constants according to Vlassak et al.[27]. Exemplary AFM micrographs and calculated root-mean-square (RMS) surface roughness S_q are illustrated in Fig. 3. An Olympus AC-160TS cantilever was therefore applied. Insets depict smaller scanning areas of 100 nm in lateral size. They were acquired with a Bruker Icon V AFM using high resolution Bruker SCANASYST-AIR AFM probes ($R_{tip} \approx 2$ nm).

3 Results and Discussion

3.1 Significance of FEA

The first part of this section will give a brief review of the FEA approach. Its predictive power concerning the dispersion relation behavior as well as the influence of linear elastic lateral shear forces will be put under scrutiny. Therefore, the first two contact resonances of the NCLR-1 and Tap190-2 are acquired on all four references at two tip blunting states each. Experimental results can be taken from Fig. 4. For NCLR-1, the first cycle is omitted here, since notable changes

during measurement occurred. However, contact resonances for second and third cycle match well within the errors. For all other measurements (e.g. for Tap190-1 Fig.4), three cycles were nevertheless performed and show satisfactory agreement as well [†]. The second step involved the calculation of k for both eigenmodes via dispersion relations given in Fig. 2. If both dispersion curves yield similar k within the experimental CR-AFM errors, the relative curve propagation behavior, predicted by FEA, can be considered as reasonable and the value of k will properly represent the contact stiffness acting on the probes. The whole procedure was repeated for $k_{lat} = 0.75\,k$. This commonly used relation is motivated by definition $k_{lat} := 8\sqrt{A_c/\pi}\,G$ and shear deformations in tip and specimen due to the lateral displacement fraction of excited cantilevers. Focusing on the case, where k_{lat} is neglected, quite satisfactory agreement can be obtained for both probes and blunting states. For less blunted tips however, a slight systematically growing discrepancy is recognizable with increasing specimen indentation moduli. The consideration of a lateral contact stiffness k_{lat} leads to a systematic vertical shift well beyond the error bars, where values extracted from the second contact resonance underestimate k with respect to the first one. In general, this effect related to k_{lat} can be traced back to each eigenmode's characteristic bending geometry. A vertical beam deflection u_z around its equilibrium position always comes along with a lateral displacement component u_x as well. In case of the second vertical bending eigenmode, the fraction u_z/u_x at the cantilever tip is about four times smaller than that of the first eigenmode, resulting in an increased sensitivity to lateral shear forces associated with k_{lat}. The slope of second mode's dispersion relation thus increases more upon introduction of k_{lat}. Concerning the deviation of both modal predictions, two possible explanations shall be given at this point. The first one refers to the common utilization of k_{lat}


[†] The experienced reader might realize a reduced contact resonance for STO, compared to other specimens, which is due to Tap190-2 measurements performed after having subjected STO to severe heat treatment under ambient conditions. STO is well known for heat-induced structural surface reconfiguration processes such as changes in Sr/Ti-ratio and metal segregation mechanisms (see e.g.[34] and references therein) which may affect indentation modulus as well.
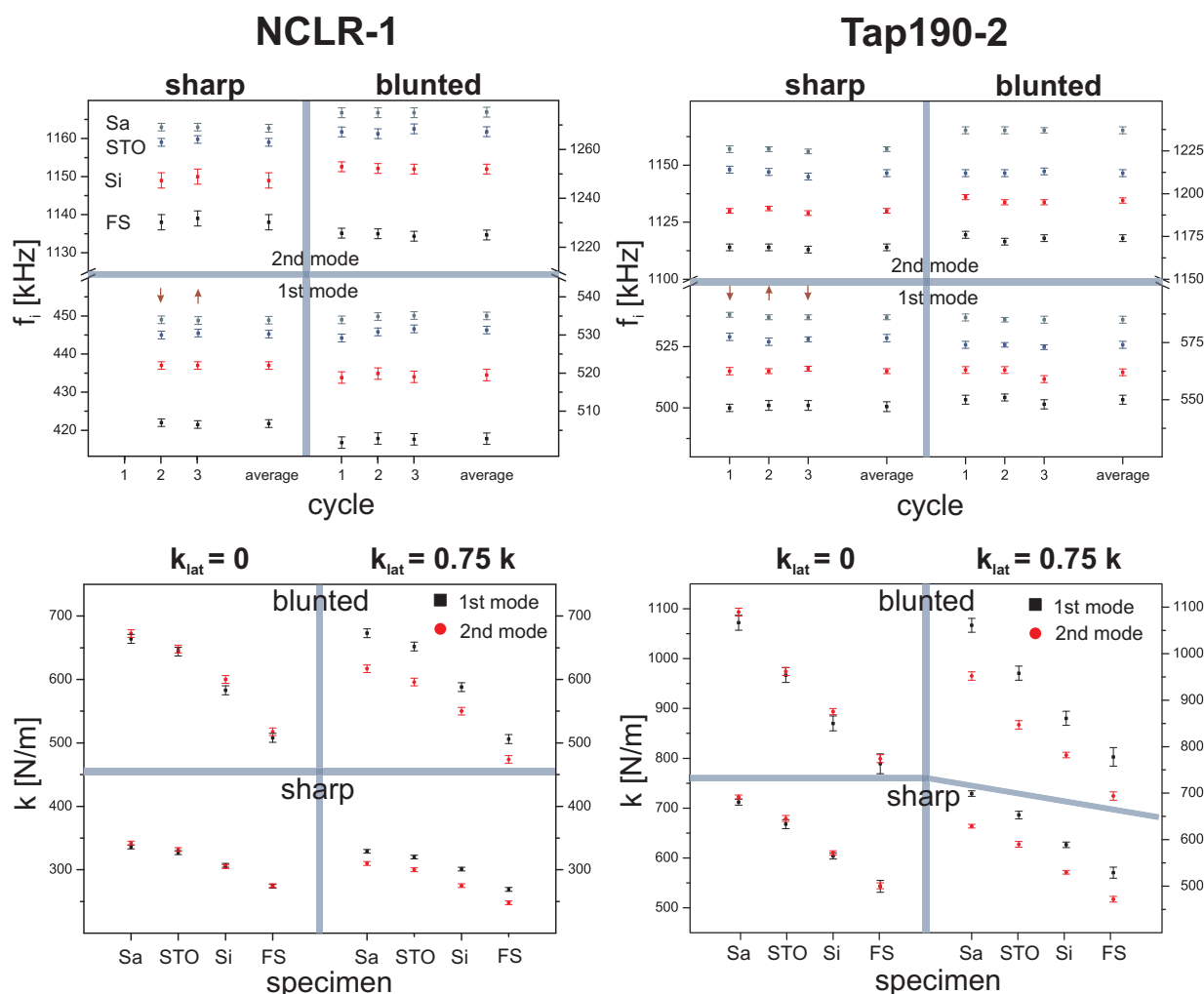
Fig. 4 Top: Experimental CR-AFM results of point-map cycles on four reference samples. Small arrows indicate the measuring order. Bottom: Predicted contact stiffness k of the first two eigenmodes using dispersion relations given in Fig. 2 and optionally $k_{lat} = \{0, 0.75\,k\}$ N/m. Data sets refer to the NCLR-1 (left) and TAP190-2 (right), respectively.

in combination with a simplified analytical rectangular beam model similar to the one described in section 2.1. Besides the aforementioned inaccuracies concerning free eigenfrequency predictions, it additionally lacks consideration of tip mass and elasticity. Contact forces acting on the tip are consequently redirected in a more rigid fashion to the probe beam. As explained before, the presence of a lateral contact spring affects each eigenmode's dispersion relation differently. The shear stiffness k_{lat} could then just degenerate to a technical correction parameter for relative dispersion behavior adjustments of the analytical model. A second possible interpretation considers the tip-surface interaction itself. The tip is only loaded onto the specimen surface but not rigidly fixed and the beam-shaped geometry of a vertically oscillating AFM probe results in a torque acting on the tip-surface contact. This torque in

turn might preferentially lead to lateral apex slipping at the surface rather than shear deformations as also suggested in [35]. A further explanation will be given later with regard to the applied contact model. To conclude this section, we thus emphasize that our FEA calculations exhibit good agreement with experimental dispersion relations of the first two bending modes without any need of a lateral shear force constant k_{lat}. This finding is well supported by further combined experiments and FEA simulations with other Tap190 probes as well as two modern NCLR probes having a different geometry than NCLR-1 (not discussed herein) and agrees with findings in [36]. We thus believe, that fit parameters $\{n, M_{tip}\}$ gained in the present study have to be interpreted with regard to physical processes occurring in the contact region.

NCLR-1 (2nd mode)

Tap190-1 (2nd mode)
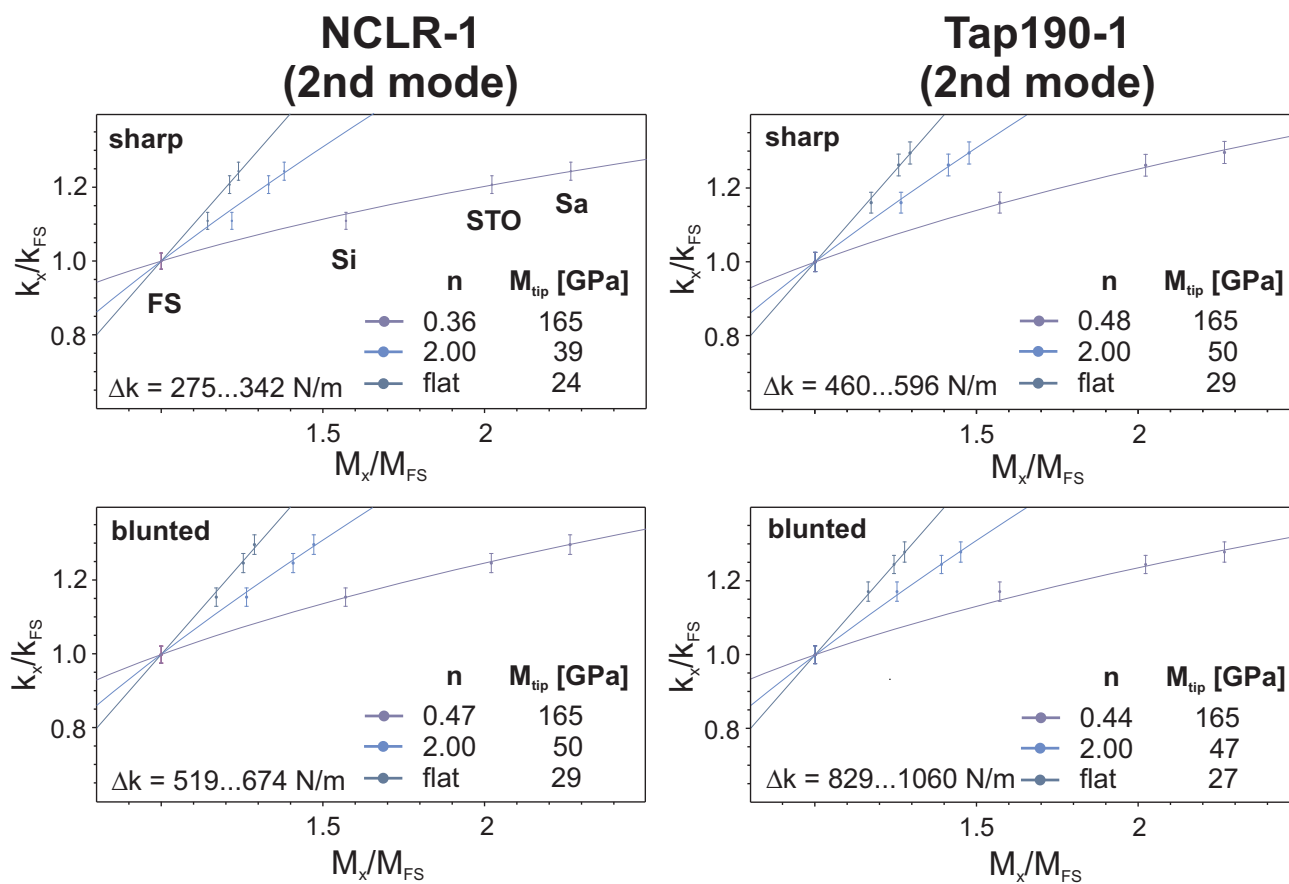
Fig. 5 Contact stiffnesses k_x - obtained from experimental contact resonances f_i of NCLR-1 (Fig. 4) and Tap190-1 (Fig. 7) and known probe dispersion relations $f_i(k)$ - plotted over tip-sample system indentation moduli M_x. Data is normalized to that of FS (normalization to other references is, however, also possible). Corresponding fit curves base on Eqs. 4 and 6 while fitting occurred via n and M_{tip}. Shown are curves for the three cases $n \to \infty$ (flat punch), $n := 2$ (parabolic tip) and $M_{tip} := 165$ GPa. Contact stiffness spans $\Delta k = k_{FS}...k_{Sa}$ contain information about contact areas and shall give a relative impression between both probes and tip blunting states, respectively.

3.2 Reviewing the contact model

3.2.1 Bare Si tips. This section treats the second step of quantitative data extraction, where Eq. 6 is applied to fit discrete experimental data points $\{k_x, M_x\}$ via parameter pairs $\{n, M_{tip}\}$. Data points are normalized to those obtained for FS, where M_{FS} is the corresponding tip-sample system modulus given by Eq. 4. We therefore assumed three cases: (i) a flat punch tip geometry ($n \to \infty$), (ii) a parabolic tip profile ($n := 2$) and (iii) a tip indentation modulus similar to the expected bulk value of Si ($M_{Si} := 165$ GPa). The following data analysis resides on experimental results obtained with bare Si probes NCLR-1 (already shown in Fig. 4) and Tap190-1. Analogue experimental results of Tap190-1 are shown in Fig. 7 since they are needed for a later comparison. However, Fig. 5 summarizes all relevant results for the following discussion. Data fitting was realized using a standard χ^2 minimization algorithm[37], where data points representing Si were intentionally disregarded for reasons explained in a later part of this work. At first glance, one might conclude that all three assumptions concerning tip characteristics lead to satisfying agreement between experimental data points and fits. This important information agrees well with results of previous careful work (e.g.[20,21]). Focusing on experimental results given in Figs. 4 and 7, comparable small contact resonance differences between Sa and STO are due to their superior elastic properties with respect to tip material. Relative errors therefore increase notably beyond STO. This conclusion is valid for both probes and blunting states, respectively. It in turn means, that the multi-reference approach with utilized tips allows for quantitative mechanical determination within an elasticity regime of about $50 - 300$ GPa. Diagrams of Fig. 5 also highlight obtained fit parameter pairs $\{n, M_{tip}\}$ as well as information about the contact stiffness interval Δk of each tip blunting state.

A comparison of these regimes shows that the sharp NCLR-1 tip is the sharpest of the whole set and associated tip-contact area is therefore the smallest. The blunted NCLR-1 tip state is slightly increased compared to the sharp one of Tap190-1 but both overlap over a wide range. In contrast, the blunted Tap190-1 tip forms the largest contact area once loaded to a specimen surface. In fact, diagrams starting from sharp NCLR-1 to blunted Tap190-1 represent a series of increasing tip wear. Following this abrasion path, a slight relative shift of Si data points with respect to fit curves is recognizable. Where fit curves for the lowest NCLR-1 blunting state overestimate Si response for all assumed tip characteristics, the Si data set approaches simulated curves of the two overlapping medium blunted states. Both, NCLR-1- and the Tap190-1 data are generally very similar for all specimens. Finally, experimental data related to Si slightly exceeds computed curves in the last case of maximum tip wear (blunted Tap190-1). However, since the shift occurs almost within error bars this finding lacks in significance. Moreover, the aforementioned proximity of contact resonances related to the two stiffest specimens STO and Sa, allows the χ^2-fit to match all points within experimental deviations - even if Si data is considered as well. The weak trend obtained here, is nevertheless supported by more resilient results gathered with DLC coated probes and discussed in the last section.

Focusing now on utilized fit parameter pairs $\{n, M_{tip}\}$, leads to the conclusion that both, the assumption of a parabolic tip as well as a flat punch results in dramatic underestimations of tip indentation moduli in all cases. The consideration of Si data points for data fitting has only a minor influence and does not affect this finding. Although reduced tip indentation moduli $M_{tip} \approx 100$ GPa are reported in literature and may be correlated to tip oxidation- and amorphization processes[20,21], recent values cannot be explained just by this consideration. All presented results exhibit very similar parameter pair configurations, which in turn hints at similar geometric tip configurations. The assumption of more realistic mechanical properties, such as the aforementioned bulk value of Si, necessitates shape parameters n to be set well below 1. This would correspond to a power functional describing a spike-like tip shape profile. Obviously, a direct investigative approach is inevitable in order to get conclusive knowledge about apex geometry. We therefore used SEM to image utilized AFM tips from different perspectives. Within typical resolution limits of about 2 nm, this technique should at least provide an initial clue about desired tip features. Figure 6 a) yields exemplary SEM micrographs obtained for the Tap190-1 AFM probe. The illustrated side- and top views are acquired directly after CR-AFM investigations and represent the blunted wear-off state associated with results given in Fig. 5. An almost perfect flat punch geometry can be seen, with a smoothed triangular base area determined by the pyramidal AFM tip. Moreover,

the side view reveals the abraded face to be tilted about 10.9° (note that the whole cantilever was aligned horizontally in this image), which is nearly identical with the overall probe tilting angle due to mounting. Further SEM measurements carried out on Tap190-2 and two more SEM probes (not shown in this study) yield the same information. The result can thus be regarded as being representative for all experiments done with bare Si tips in this work and in turn agrees well with the aforementioned similarity of fit parameter pairs $\{n, M_{tip}\}$ given in Fig. 5. The preferable generation of the flat stamp is due to the applied blunting procedure (see section 2.3) and the intrinsic soft amorphous oxide layer, which steadily arises once a previous is abraded. However, the presence of this specific apex characteristic leads to the most pronounced deviation from expected indentation moduli. Reasons for this discrepancy might be either found in (i) pure mechanical modification related to lattice structure or (ii) deviations between real contact physics and assumptions related to the applied contact model. Besides a thin natural amorphous oxide layer, other effects correlated to (i) may principally influence M_{tip} of nano meter sized apices. Among those is the growing surface to volume ratio, where the relative amount of surface atoms - characterized by reduced binding symmetry - gets notable. Stress induced lattice recombination mechanisms constitute one further probable effect related to (i). However, concerning the first mentioned phenomenon, AFM tip dimensions are still too high. Lattice recombiantions were subject to extensive previous research and it is well known that Si undergoes a metal transition to β-tin phase whereas an additional bcc phase may arise upon stress release[38,39]. Necessary pressures, however, exceed those applied in CR-AFM by far. We therefore focus on more obvious and intuitively expected causes related to (ii). As generally known, Eqs. 5 and 6 rely on the Hertzian contact model, which disregards friction and - even more important - assumes perfectly smooth surfaces as well as small stress field extensions with respect to the body dimension and finally constitutes a non-conforming body approach (changes in surface curvature upon loading are neglected). An estimation of typical surface deformations arising for presented CR-AFM experiments, shall clarify if these conditions are violated. Together with definition 3, known tip load F_l and Eq. 4, the cumulative deformation (displacement) d of the tip-surface system can be calculated for a flat punch geometry. Referring to Fig. 6 a), a lower boundary of the Tap190-1's abraded tip area can be estimated to $A_c \approx 750$ nm^2 and constitutes the contact area for perfectly smooth tip- and sample surfaces as well. Assuming tip indentation modulus M_{tip} to equal the bulk value of Si, displacement ranges from $d = 1.6$ Å (Sa) to $d = 3.8$ Å (FS). According to Johnson[40], the Hertz contact theory is a good approximation as long as a randomly rough surface - represented by its RMS value - remains below 5% of d. Considering extracted RMS roughness
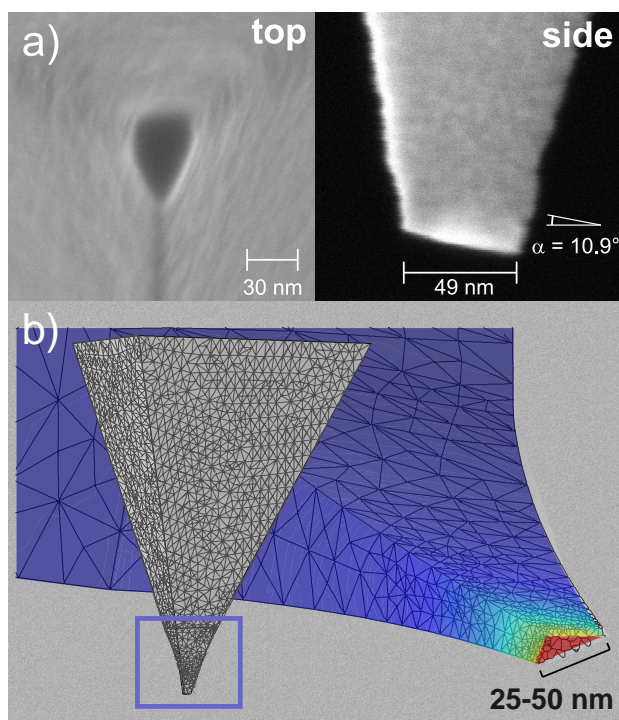
Fig. 6 a) SEM micrographs of blunted Tap190-1 tip apex, related to the last diagram in Fig. 5. Probe tilting due to cantilever mounting causes the blunted flat stamp to have an angle of about 11° with respect to the image horizontal. b) Detailed FEA model of tip- and apex geometry. Color coded volume represents normalized vertical displacement field upon loading.

from previous AFM topography measurements - highlighted in Fig. 3 - one may indeed conclude that this condition is seriously violated. Focusing on spatially high resolved AFM micrographs (see inset of Fig. 3), reveals roughness features with lateral sizes well below tip dimension causing the occurrence of multi-asperities between tip and surface. A neglect of surface curvature changes upon loading may thus be locally violated as well. As a consequence, the Hertz model would overestimate contact area systematically. Relation 6 in turn becomes questionable as soon as the load functional $F_l(A_c)$ depends more critically on individual surface properties like RMS-roughness and corresponding lateral distribution – represented by the power-spectral-density (PSD) function. Discrepancies arising between these specimen-related quantities additionally contribute and influence effective values of M_{tip} and shape parameter n. However, if this effect would suffice to explain the observed artificial values of M_{tip}, it should weaken with reduced tip sizes since indentation depth increases with reduced lateral tip extension (still presuming a flat punch Si tip). Referring to medium blunted tip states of NCLR-1 and Tap190-1, the average contact stiffness of all specimens re-

duces roughly by a factor of 2 (see. Δk in Fig. 5) with respect to the aforementioned blunted Tap190-1 tip. In case of the smallest tip-wear - naming sharp NCLR-1 - the ratio even amounts to about 3. According to Eq. 3, k scales linearly with lateral tip size as well and one may assume an increase of the aforementioned sample specific displacements d by the same amount. In contrast, neither the medium blunted tips nor the the smallest exhibit less artificial M_{tip}. Concerning the latter one, M_{tip} reduces even further. Although roughness is found to violate condition $S_q \leq 0.05\,d^{40}$, it can be excluded as possible reason for apparently low values of M_{tip}. Hence, another condition of Hertz contact theory must be critically examined. We therefore emphasize again the assumption of small stress field extensions with respect to the tip size. This prerequisite is intrinsically critical for a flat punch geometry since contact area is directly given by its lateral extension. While the specimen may be regarded as an infinite elastic half space, the tip geometry is of reduced symmetry and lacks any surrounding stabilizing matrix material outside the contact region. This fact can be considered a static problem and needs to be taken into account - regardless of the absolute contact pressure p_m. Similar to the introduction of an cantilever stiffness k_c, the tip stiffness k_{tip} additionally owes to its shape $\xi(\vec{x})$ and relation Eq. 4 modifies to

$$\frac{1}{M} = \underbrace{\sqrt{\frac{A_c}{\pi}}\frac{2}{k_{tip}(\xi(\vec{x}),M_{Si})}}_{\frac{1}{M_{tip}}} + \frac{1}{M_s} \qquad (7)$$

where the first summand substitutes tip material modulus M_{tip} due to statics and shall converge to the true material value M_{Si} if vertical and lateral stress field components remain within tip volume. Although an effective body stiffness hides behind this term, we nevertheless keep the notation M_{tip} in the following. Figure 6 b) highlights the situation on a modeled Si flat punch tip. It exhibits the pyramidal base area as well as similar apex features like the real counterpart. Stationary FEA analysis were performed for two truncated apices - a blunted one in accordance to 6 a) (Tap-1 blunted) and a second addressing less abrasion alike blunted NCLR-1 and sharp Tap-1 (lateral tip dimension was estimated to 25 nm). The applied vertical load again amounts to $F_l = 500$ nN. Similar to FEA computations of entire AFM cantilevers, only one half of the tip was simulated considering a symmetry plane in order to optimize mesh density within computational limits. Extracted vertical displacements u of apex surface, known A_c and definition 3 finally yield effective tip indentation modulus. One obtains $M_{tip} = 33$ GPa for the larger virtual tip and 25 GPa in case of the smaller one. These values are indeed very similar to experimental fit data given in Fig 5. Furthermore, both computed values are comparable close to each other - identically to the experiments and despite a factor of 6 between both flat
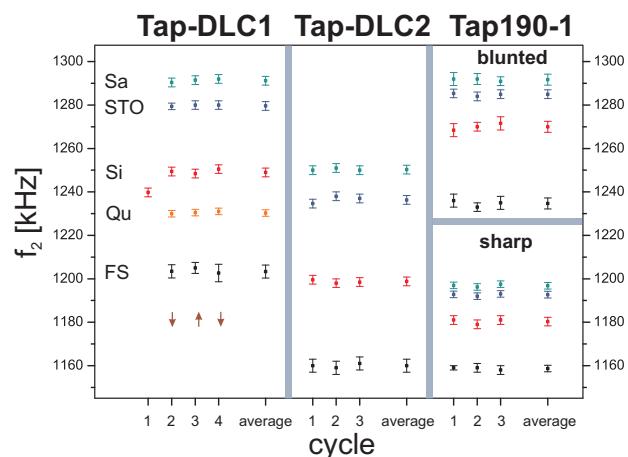
Fig. 7 CR-AFM point map cycles of 2nd contact resonance acquired with two DLC coated AFM probes (left, center) and a non-coated probe at two different tip blunting states (right). Red arrows indicate the measuring order.
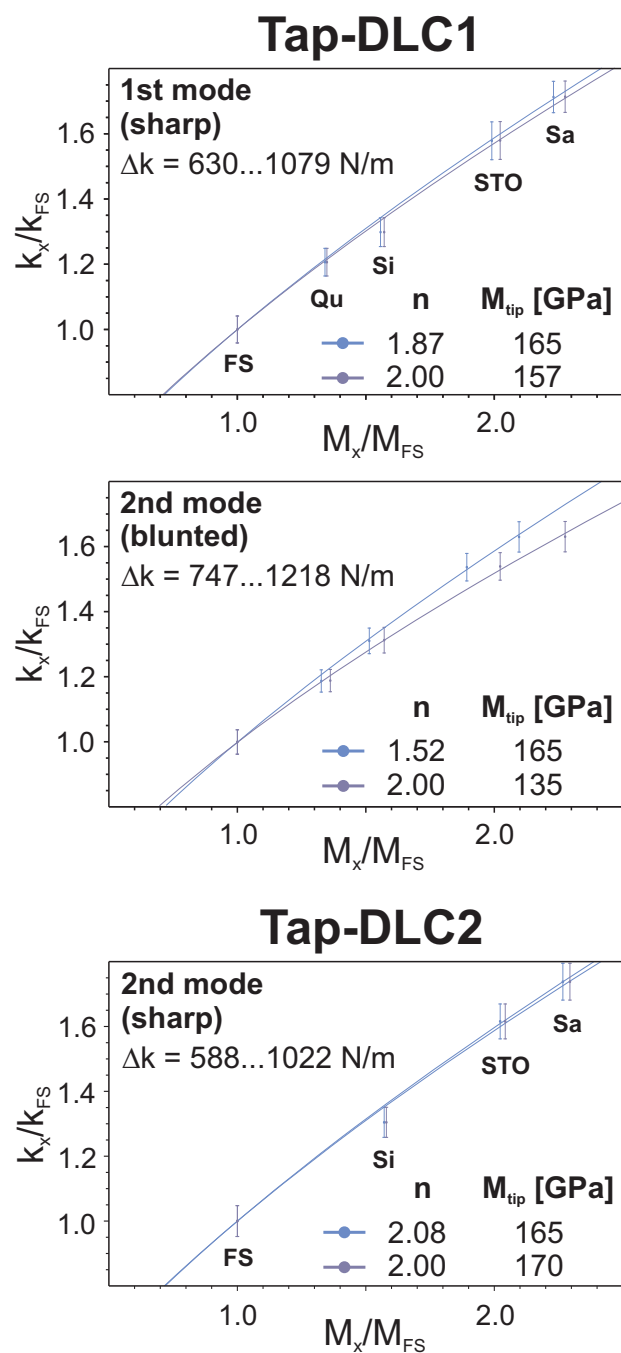
apex areas. Obviously, the violation of negligible small stress field extensions - as a result of particular tip geometry - can be finally identified as the major origin of affected M_{tip}. Similar tip aspect ratios generate these specific mechanical characteristics and are subject to the next section.

Referring back to the lateral contact shear stiffness k_{lat} and its negative impact on computed FEA cantilever dispersion relations, the argument of tip statics also causes an effectively softened shear modulus G_{tip} and might justify the negligence of k_{lat}. Indeed, further stationary lateral FEA analysis of both truncated tip apices revealed the static lateral tip stiffness $k_{tip,lat}$ to remain below 7% of the vertical counterpart k_{tip}. As a consequence, the accumulated lateral contact stiffness $k_{lat} = (k_{tip,lat}^{-1} + k_{s,lat}^{-1})^{-1}$ is mainly determined by the soft static tip fraction and barely contributes to overall tip-surface interaction. Even though contact phenomena like tip gliding do not occur, tip statics would constitute the major limiting factor of k_{lat}.

As initially intended, the presented discussion provides a reasonable explanation for obtained tip indentation modulus of the applied contact model. These findings are strengthened by experiments based on coated tips and further investigated as presented in the following.

3.2.2 Impact of DLC coating. Figure 7 illustrates experimental results, carried out with two DLC coated AFM probes TapDLC-1 and TapDLC-2 on the same reference samples. Additionally, data of the Tap190-1 - subject to the previous section - is presented and consulted for comparison. TapDLC-1 was slightly abraded between measurements carried out with the first and the second contact resonance, respectively. This is already indicated by the vertical offset between resonance

frequency intervals related to both coated probes. Results obtained with the first eigenmode are not included in Fig. 7 but are of similar significance like illustrated data. More essential, however, is the fact that both probes with protective coating exhibit a significantly larger contact resonance span across the entire reference sample set. In order to avoid incorrect data interpretation, Tap190-1 was chosen for comparison, since it yields a beam stiffness k_c very similar to that of TapDLC-2 (see Table 1) and an almost identical dispersion relation. Not explained in detail within the previous section, tip blunting of Tap190-1 was moreover optimized in a manner that the contact resonance of FS matches the associated one of TapDLC-2 - as shown in Fig. 7. The overall contact resonance span of the coated TapDLC-2 exceeds that of the bare counterpart by a factor of two, whereas especially sub-distances between the three harder materials raise. This is solely related to contact physics and synonymous with an increased mechanical sensitivity by the same amount. The answer of this remarkable phenomenon is closely related to modified elastic tip properties and provided after a more detailed discussion of the latter mentioned. Therefore, results of the data fit procedures via parameter set $\{n, M_{tip}\}$ and similar conditions assumed for bare Si probes are shown in Fig. 8. Focusing on results of sharp TapDLC-1 cantilever, all five experimentally obtained data points can be fitted well, whereas the necessary fit parameter M_{tip} is much more intuitive than those of Si tips. Situation is quite similar for the blunted TapDLC-1 and TapDLC-2, whereas the Si reference sample again appears to be slightly softer for both sharp DLC tip states than theoretically expected. As depicted in Fig. 9, SEM micrographs are taken from both apices to get an idea about the predictability of applied Hertz model. Additionally, images are overlaid with tip profile plots based on Eq. 2 and obtained shape parameters n for condition $M_{tip} = M_{Si} = 165$ GPa. Interestingly, a very good agreement between calculated and real tip profiles can be found, which basically states that tip indentation moduli are at least close to the expected bulk value of Si within experimental errors. At first glance, this result might be confusing and appears to be coincidence, since polycrystalline DLC should exhibit significantly different indentation moduli than Si. Indeed, no detailed information of real DLC film thickness and associated Young's modulus is available for these commercial tips. However, extensive work has been raised in the past to determine various properties like hybridization degree and elasticity of deposited DLC films (e.g.[41]). Depending on deposition conditions, Young's modulus may take extremal values of $16 - 450$ GPa but is typically determined to lie roughly around 100 GPa[41–45]. We therefore applied further stationary two-dimensional FEA simulations of simplified tip geometries. A radial symmetric Si cone of height h and opening angle θ represents the cantilever tip, whereas its apex is optionally truncated or of spherical shape as shown in Fig. 9 b).

Tap-DLC1

1st mode (sharp)
$\Delta k = 630...1079$ N/m

	n	M_{tip} [GPa]
	1.87	165
	2.00	157

2nd mode (blunted)
$\Delta k = 747...1218$ N/m

	n	M_{tip} [GPa]
	1.52	165
	2.00	135

Tap-DLC2

2nd mode (sharp)
$\Delta k = 588...1022$ N/m

	n	M_{tip} [GPa]
	2.08	165
	2.00	170

Fig. 8 As described in Fig. 5, similar normalized plots of k_x vs. M_x are shown for the two DLC coated AFM probes. Contact stiffnesses k_x were again extracted from experimentally obtained contact resonances f_i (Fig. 7) and individual FEA probe dispersion relations $f_i(k)$. A quartz sample constitutes a fifth reference for experiments with TapDLC-1.

The first mentioned corresponds again to a simplified Si flat punch - similar to that discussed in the previous section. The spherically ended cone accounts for tip shape of TapDLC-2 (see Fig. 9 a)). For these two bare Si cones, apparent tip indentation moduli M_{tip} were computed depending on cone opening angle θ. The procedure was exemplary repeated for the spherical ended cone exhibiting additional coatings of 100 GPa and 350 GPa at 15 nm film thickness as well as 100 GPa at only 5 nm, respectively. They shall represent lower and upper limits of expected mechanical influences arising from a DLC film. Poisson ratio was chosen to be $\nu = 0.25$ and shall represent an average of literature values [43,44]. The overall apex sphere radius remained constant at 25 nm and the load amounts to $F_l = 500$ nN in all cases. Figure 9 c) depicts calculated data of $M_{tip}(\theta)$ normalized to M_{Si}. The truncated Si cone of flat circular contact radius of $a_c = 25$ nm again reveals a dramatically reduced tip indentation modulus for small opening angles - consistent with aforementioned results of three dimensional FEA calculations. Values indeed converge towards bulk Si data with growing θ. Figure 6 b) exemplary highlights normalized pressure distributions within indenter and loaded block. Where the truncated cone shows significant pressures at its boundaries, associated field of the block completely fades within material volume. Viewing on the spherically ended Si cone, one easily realizes clearly increased M_{tip} at low θ compared to the truncated counterpart. Additionally, Fig. 9 b) highlights corresponding pressure distribution which fades almost completely within tip volume, whereas the contact radius amounts to only 3.9 nm. The difference ΔM_{tip} between both bare Si cones is indeed the result of deviating stress field characteristics in both cone apices, where the sphere turns out to be less sensitive to cone geometry connected with θ. Slightly lower values of M_{tip} at elevated opening angles can be traced back to the same origin. Sphere curvature mainly determines mechanical response and the comparable high load leads to a small but non-negligible deformation associated with elevated stresses at the indenter surface. However, similar computations with reduced loading forces F_l reveal M_{tip} to converge closer to M_{Si}. Nevertheless, both Si cones exhibit a dramatic softening behavior once θ tends to $0°$. This trend is mainly driven by definition 3 and the general Hook's relation of elasticity theory $\sigma = Y \varepsilon$ - necessitating M_{tip} to be replaced by the effective body stiffness according to Eq. 7. Since load keeps constant for simulations, the contact area and thus stress σ and strain ε remain constant as well for a given θ. The absolute strain Δh, however, grows with increasing cone height h. Consequently, $2M_{tip} a_c := k_{tip} \approx \Delta F/\Delta h = Y_{Si} A_c/h$ converges to zero at $\theta = 0°$. In other words, an indenter of constant cross sectional area - describable as a series of springs - gets infinite soft with increasing chain length $h = N h_i$ since its overall stiffness sums only inverse proportionally with spring number N. Once θ exceeds zero, a growing cross sectional cone area $A(z)$ partially compensates this behavior (increasing amount of parallel spring coupling) and leads to finite values
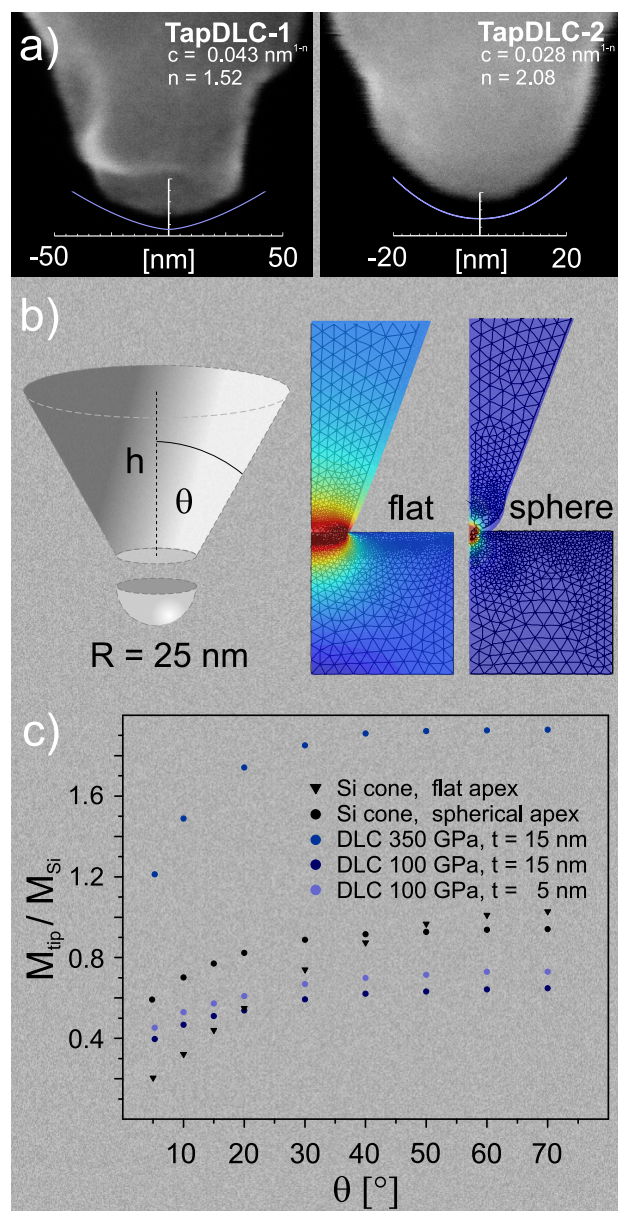
Fig. 9 a) SEM side views of the two DLC coated probes TapDLC-1 and TapDLC-2, respectively. Tip profiles according to Eq. 6 and fit results given in Fig. 8 are overlaid. b) A radial symmetric cone for FEA investigations being optionally truncated or spherically ended. Pressure distributions upon loading are shown for both cases. c) FEA results of apparent M_{tip} vs. cone opening angle θ.

close to predefined parameters of each film. Even a notable thickness reduction to only 5 nm, in case of the 100 GPa coating, results in a comparable small relative increase of about 10%. It shall be pointed out here, that the rigid coupling of tip material and coating - as assumed for FEA - not necessarily reflects real interface physics. Nevertheless, the comparison of experiments and computed data allows some general conclusions. The presented DLC coating surely exhibits an increased Young's modulus and durability compared to an amorphous 2 nm thin intrinsic SiO_x layer but, however, does not exceed the bulk value of Si notably. This finding agrees with commonly obtained results given in [43–45]. Furthermore, the FEA-based comparison of bare Si cones with truncated and spherical apices, respectively, state that optimum $\{n, M_{\text{tip}}\}$-data pairs gained with DLC coated tips are found in the preservation of a notable and well defined tip surface curvature (e.g. parabolic shape) rather than superior DLC material properties. This in turn ensures the overwhelming part of stresses to fade within tip volume - satisfying preconditions of Hertzian theory.

Referring now to the mechanical sensitivity of CR-AFM, we consult again Eq. 6 for the contact stiffness ratio of two arbitrary specimens x and y. One can easily proof that k_x/k_y increases with raising tip indentation modulus, resulting in larger contact stiffness spans Δk. Since dispersion relations of AFM probes are strictly monotonous growing functions (see Fig. 2), this applies for the associated contact resonance span as well and explains the increased sensitivity of DLC coated tips. The usage of stiffer tips thus enhances mechanical resolution of an AFM probe under otherwise identical conditions (such as contact dimension and probe dispersion $f_i(k)$). It is also noteworthy, that increasing contact area has a similar effect but is, however, undesired since it is at the cost of spatial resolution. Measuring errors due to growing sensitivity to surface roughness may raise as well.

Once again, we refer to typical indentation displacements achieved with presented DLC probes. According to Yamanaka et al. [19], the displacement functional for a polynomial shaped tip profile given by Eq. 2 yields 1.3 nm $= d_{\text{FS}} \geq d \geq d_{\text{Sa}} = 0.75$ nm for TapDLC-1 and 1.5 nm $\geq d \geq 0.85$ nm for TapDLC-2. These values exceed nominal counterparts of the flat blunted Tap190-1 tip by factors of 3 and beyond, whereas contact radii a_c are furthermore below 7 nm for both coated probes. A highly reduced artificial impact of roughness is the consequence. Sufficient RMS roughness analysis for lateral surface features close to contact dimensions is not possible due to limitations of available tips. The aforementioned condition $S_q \leq 0.05 d$ is probably still not fulfilled. However, from recent results with DLC coated tips we conclude that, as long as individual RMS roughness and associated PSDs of different specimens do not deviate too much, similar load functionals $F_l(A_c)$ may be assumed and allow the application of Eq. 6. A

$M_{\text{tip}} > 0$. This pure geometric influence - related to the tip aspect ratio and associated effective body stiffness - becomes finally negligible for high cone angles θ. Focusing now on M_{tip}-data plots of coated cones with spherical apices, curve propagation is similar to that of a bare Si cone. Indentation modulus saturation at high angles θ, however, occurs very

violation of the Hertz model presumption concerning surface roughness is then less critical.

We finally view again on the aforementioned apparent indentation modulus increase of the Si specimen with proceeding tip-wear. Although previous experiments with non-coated tips lack conclusiveness due to experimental uncertainties, a systematic trend was nevertheless observed for other probes not discussed herein. As can be taken from Fig. 7, CR-AFM experiments under usage of TapDLC-1 additionally contain data of a quartz single crystal (see table 2). Artificial data analysis, due to inaccuracies of cantilever dispersion relations, are unlikely for two reasons: (i) both sharper DLC probes yield reduced elastic response of Si but were acquired with different contact resonances; and (ii) Qu exhibits M close to Si but corresponding data remain unaffected for both tip blunting states of TapDLC-1. These more resilient results strengthen the assumption of real stiffening processes on Si surfaces with increasing contact area and agrees with the fact, that Si represents the only sample of the specimen set which is not an inert oxide ceramic under ambient conditions but tends to create an amorphous surface oxide layer. Since stress field extension generally scales with the contact area of two loaded bodies, more abraded tips thus lead to a larger volume extension of stresses and a bulkier material response. With growing response fraction of the buried non-affected single crystalline Si, M_{Si} converges to the bulk value as well.

4   Conclusions

The presented work dealt with influences on contact mechanics at the nano scale and addressed their impact on quantitative mechanical CR-AFM investigations. A combined approach of extensive FEA computations and a contact model with adjustable parameters n (shape index) and M_{tip} (tip indentation modulus) was applied for this purpose. The investigative scope involved the artificiality of mechanical tip properties arising from multi-reference based quantitative CR-AFM analysis. It turned out that individualized extensive FEA of utilized AFM probes, provides good predictions concerning dispersion relations of the first two contact resonances. These observations distract the cause of apparent tip properties to the applied contact model and related physics. Vice versa, this means that n and M_{tip} do not degenerate to insignificant correction parameters owing to inaccuracies of the cantilever beam model but may be regarded as effective values due to real physical processes arising at the contact. Indeed, systematic quantitative CR-AFM analysis as well as sample topography determination and stationary FEA tip modeling identified the surface roughness and tip statics as critical factors violating fundamental demands of the Hertzian contact model. The latter is correlated to (i) stress fields - arising at the contact interface - and their extension with respect to lateral tip dimen-

sions, as well as (ii) the overall tip aspect ratio. Static influences turned out to be the dominant cause of apparent indentation modulus M_{tip}. Together with probe dispersion relation analysis, this finding furthermore proves the redundancy of a lateral shear contact stiffness k_{lat} for presented Si tips - even if no tip gliding occurs. The impact of sample surface roughness can be considered less critical, as long as a set of specimens exhibits similar roughness characteristics (determined by corresponding RMS values and PSD). The Hertzian contact model regains its strict significance in the presence of a protective DLC tip coating, whereas tip indentation modulus M_{tip} takes values close to bulk Si. This is mainly due to the polynomial shaped tip profile which ensures contact stresses upon loading to fade within tip material volume. Improved mechanical elasticity of utilized DLC films plays a minor role for this phenomenon. Furthermore, enhanced indentation depths associated with lower contact areas in turn reduce sensitivity to artifacts arising from roughness features. It could be also shown, that mechanical resolution of CR-AFM increases notably under usage of such effectively hardened tips. Furthermore, the indentation modulus of the Si reference specimen exhibited a dependency on tip-surface contact area. We address this phenomenon to the intrinsic surface oxide layer arising under ambient conditions. Increasing contact area is associated with larger volume extensions of stress fields and results in a reduced relative fraction of mechanical response related to the layer. The indentation modulus consequently converges to the Si bulk value. However, in accordance to [20,21], less effort in probe modeling is still sufficient for quantitative nano mechanical analysis of conventional materials as long as a multi-reference sample approach is used. The strict proof of apparently low M_{tip} due to tip statics shall finally convince to turn away from single-reference based quantitative CR-AFM investigations. Detailed information about tip properties n and M_{tip} become essential once more elaborated quantitative mechanical analysis of complex heterogenic nano systems - like e.g. buried structures - is center of interest, since such investigations necessitate detailed knowledge about stress fields arising in contacting bodies.

5   Acknowledgments

References

1 G. Binnig and C. F. Quate, *Physical Review Letters*, 1986, **56**, 930–933.

2 Y. Martin and H. K. Wickramasinghe, *Applied Physics Letters*, 1987, **50**, 1455.

3 Y. Martin, D. W. Abraham and H. K. Wickramasinghe, *Applied Physics Letters*, 1988, **52**, 1103.

4 U. Rabe and W. Arnold, *Applied Physics Letters*, 1994, **64**, 1493.

5 K. Yamanaka, H. Ogiso and O. Kolosov, *Applied Physics Letters*, 1994, **64**, 178.

6 U. Rabe, S. Amelio, E. Kester, V. Scherer, S. Hirsekorn and W. Arnold, *Ultrasonics*, 2000, **38**, 430–437.

7 P. A. Yuya, D. C. Hurley and J. A. Turner, *Journal of Applied Physics*, 2008, **104**, 074916.

8 J. P. Killgore, D. G. Yablon, A. H. Tsou, A. Gannepalli, P. A. Yuya, J. A. Turner, R. Proksch and D. C. Hurley, *Langmuir*, 2011, **27**, 13983–13987.

9 G. Stan, S. W. King and R. F. Cook, *Nanotechnology*, 2012, **23**, 215703.

10 B. Pittenger, N. Erina and C. Su, 2010.

11 E. Kester, U. Rabe, L. Presmanes, P. Tailhades and W. Arnold, *Nanostructured Materials*, 1999, **12**, 779–782.

12 G. Stan, C. V. Ciobanu, P. M. Parthangal and R. F. Cook, *Nano Letters*, 2007, **7**, 3691–3697.

13 G. Stan, S. Krylyuk, A. V. Davydov, M. Vaudin, L. A. Bendersky and R. F. Cook, *Applied Physics Letters*, 2008, **92**, 241908.

14 G. Stan, C. V. Ciobanu, T. P. Thayer, G. T. Wang, J. R. Creighton, K. P. Purushotham, L. A. Bendersky and R. F. Cook, *Nanotechnology*, 2009, **20**, 035706.

15 M. Kopycinska-Müller, R. H. Geiss, J. Müller and D. C. Hurley, *Nanotechnology*, 2005, **16**, 703–709.

16 G. Stan, S. King and R. Cook, *J. Mater. Res*, 2009, 2960–2964.

17 A. M. Jakob, M. Müller, B. Rauschenbach and S. G. Mayr, *New Journal of Physics*, 2012, **14**, 033029.

18 K. Stan and R. F. Cook, *Nanotechnology*, 2008, **19**, 235701.

19 K. Yamanaka, A. Noguchi, T. Tsuji, Koike T. and T. Goto, *SIA*, 1999, **1999**, 600–606.

20 G. Stan and W. Price, *Review of Scientific Instruments*, 2006, **77**, 103707.

21 D. Passeri, M. Rossi and J. J. Vlassak, *Ultramicroscopy*, 2013, **128**, 32–41.

22 I. S. Sokolnikoff and Specht R.D., *Mathematical theory of elasticity*, 1956.

23 U. Rabe, *Ph.D. thesis*, Universität des Saarlandes, Saarbrücken, 1997.

24 M. Kopycinska-Müller, *Ph.D. thesis*, Universität des Saarlandes, Saarbrücken, 2005.

25 M. G. Larson and F. Bengzon, *The Finite Element Method: Theory, Implementation, and Applications*, Springer Berlin Heidelberg, Berlin and Heidelberg, 2013.

26 K. Geng, *Ph.D. thesis*, Universität des Saarlandes, Saarbrücken, 2007.

27 J. Vlassak, M. Ciavarella, J. Barber and X. Wang, *Journal of the Mechanics and Physics of Solids*, 2003, **51**, 1701–1721.

28 J. J. Jorgensen, *Scanning Probe Image Processor (SPIP)*, 2013.

29 Del Mar Photonics, Inc., *www.sciner.com*.

30 H. J. McSkimin, *Journal of Applied Physics*, 1953, **24**, 988.

31 R. Bell and G. Rupprecht, *Physical Review*, 1963, **129**, 90–94.

32 Moltech GmbH, www.mt–berlin.com.

33 W. C. Oliver and G. M. Pharr, *Journal of Materials Research*, 1992, **7**, 1564–1583.

34 S. F. Wagner, *Ph.D. thesis*, Universität Karslruhe, Karlsruhe, 2008.

35 F. J. Espinoza Beltran, J. Munoz-Saldanaa, D. Torres-Torres, R. Torres-Martinez and G. A. Schneider, *Journal of Materials Research*, 2006, **21**, 3072–3079.

36 J. Killgore and D. C. Hurley, *Nanotechnology*, 2012, **23**, 055702.

37 W. H. Press, *Numerical recipes: The art of scientific computing ; source code CD-ROM v 3.0*, Cambridge Univ. Press, Cambridge, V 3.0, [complete source code in C++] edn., 2007.

38 J. C. Jamieson, *Science*, 1963, **139**, 762–764.

39 R. H. Wentorf and J. S. Kasper, *Science*, 1963, **139**, 338–339.

40 K. L. Johnson, *Contact mechanics*, Cambridge Univ. Press, Cambridge u.a, 1st edn., 1985.

41 A. Grill, *Diamond and Related Materials*, 1999, **8**, 428–434.

42 A. Voevodin, M. Capano, S. Laube, M. Donley and J. Zabinski, *Thin Solid Films*, 1997, **298**, 107–115.

43 S.-J. Cho, K.-R. Lee, K. Eun, J.-h. Jeong and D. Kwon, *Diamond and Related Materials*, 1999, **8**, 1067–1072.

44 S.-J. Cho, J.-W. Chung and K.-R. Lee, *Diamond and Related Materials*, 2005, **14**, 1270–1276.

45 Y. Isono, T. Namazu and N. Terayama, *Journal of Microelectromechanical Systems*, 2006, **15**, 169–180.